ADVANCED OPTICAL MATERIALS
www.advopticalmat.de

Check for updates

Effective Passivation of InGaAs Nanowires for Telecommunication Wavelength Optoelectronics

Zahra Azimi, Aswani Gopakumar, Li Li, Felipe Kremer, Mark Lockrey, Ary Anggara Wibowo, Hieu T. Nguyen, Hark Hoe Tan, Chennupati Jagadish,* and Jennifer Wong-Leung**

Catalyst-free InGaAs nanowires are promising building blocks for optoelectronic devices operating at telecommunication wavelengths. Despite progress, the applications of InGaAs nanowires remain limited due to their high density of surface states that degrade their optical properties. Here, InGaAs nanowires with superior optical properties are achieved by effectively suppressing their surface states with an InP passivation shell. Optimal InP shell growth conditions and thickness to maximize the minority carrier lifetime are identified. The photoluminescence intensity of these passivated InGaAs nanowires is up to three orders of magnitude higher than that of their bare counterparts. Moreover, a long minority carrier lifetime of up to ≈13 ns is measured with these passivated nanowires at room temperature. Optimal passivation of InGaAs nanowires with an emission wavelength of 1530 nm results in an ultra-low surface recombination velocity of ≈280 cm s^{-1}. In addition to the shell, the crystal structure of these nanowires plays an important role in the luminescence intensity. Combined cathodoluminescence mapping and high-resolution transmission electron microscopy along the nanowires reveal significantly lower emission intensities in wurtzite predominant sections of the nanowires than zinc blende predominant ones.These insights on the optimal passivation of InGaAs provide directions for engineering high-performance nanoscale-devices in the telecommunication wavelength.

1. Introduction

Direct bandgap ternary III-V semiconductor nanowires have attracted interest for future high-performance optoelectronic devices with application in a wide range of wavelengths.[1–4] Binary III-V nanowires have selected bandgaps, limiting their use for particular wavelengths like optical fiber telecommunication wavelengths (1.3–1.55 μm).[5] Some studies attempted to extend the operational wavelengths of binary nanowires through heterostructures such as quantum dots, quantum wells, and core/shell structures.[6–11] However, the thickness and lattice mismatch of the heterostructure should be minimized to avoid the formation of detrimental strain-induced structural defects. As an alternative, ternary nanowires such as InGaAs can be used to tune the emission wavelength from 850 to 3500 nm while simultaneously minimizing the strain.

Despite progress in the growth of InGaAs nanowires, their device applications are

Z. Azimi, A. Gopakumar, H. H. Tan, C. Jagadish, J. Wong-Leung
Department of Electronic Materials Engineering
Research School of Physics
The Australian National University
Canberra, ACT 2601, Australia
E-mail: zahra.azimi@anu.edu.au; c.jagadish@ieee.org; jenny.wongleung@anu.edu.au

L. Li
Australian National Fabrication Facility ACT Node
Research School of Physics
The Australian National University
Canberra, ACT 2601, Australia

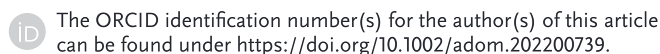
The ORCID identification number(s) for the author(s) of this article can be found under https://doi.org/10.1002/adom.202200739.

© 2022 The Authors. Advanced Optical Materials published by Wiley-VCH GmbH. This is an open access article under the terms of the Creative Commons Attribution-NonCommercial License, which permits use, distribution and reproduction in any medium, provided the original work is properly cited and is not used for commercial purposes.

DOI: 10.1002/adom.202200739

F. Kremer
Centre for Advanced Microscopy
The Australian National University
Canberra, ACT 2601, Australia

M. Lockrey
Microstructural Analysis Unit
University of Technology Sydney
Sydney, NSW 2007, Australia

A. A. Wibowo, H. T. Nguyen
School of Engineering
The Australian National University
Canberra, ACT 2601, Australia

H. H. Tan, C. Jagadish
Australian Research Council Centre of Excellence for Transformative Meta-Optical Systems
Research School of Physics
The Australian National University
Canberra, ACT 2601, Australia

© 2022 The Authors. Advanced Optical Materials published by Wiley-VCH GmbH

limited mainly due to their poor optoelectronic properties originating from a high density of surface states and the growth of imperfect crystal structures.[12–16] Reports on catalyst-free $In_xGa_{1-x}As$ nanowires demonstrate the formation of defective crystal structures with predominantly wurtzite phase at higher In content ($x > 0.7$) to predominantly zinc blende phase at higher Ga content ($x < 0.35$).[12,13] In addition to the microstructure, $In_xGa_{1-x}As$ ($0 < x < 1$) has a high surface recombination velocity (SRV) varying from ≈10^3 (InAs) to ≈5×10^5 (GaAs) cm s^{-1}.[14–16] Surface recombination dominates in nanowires with a high surface-to-volume ratio and can reduce carrier lifetime and quantum efficiency, thus limiting their optoelectronic performance. However, the surface state density can be significantly reduced by growing a shell with larger bandgap around the InGaAs core, resulting in an enhancement of the emission efficiency. Therefore, the growth of a shell on a ternary nanowire core is a promising approach to achieve both tuneable and efficient emissions.

Various III-V semiconductor shells of GaAs,[17,18] AlGaAs[11,16,19] InGaP,[4,20] InP,[21,22] InAlAs,[23] and InAsP[24] have been grown on InGaAs core nanowires with different compositions for the fabrication of optoelectronic devices. Amongst these different passivation materials, InP with a higher bandgap energy of 1.34 eV and a very low SRV of 170 cm.s^{-1} is an ideal candidate.[25] Moreover, InP is lattice-matched to $In_{0.53}Ga_{0.47}As$ and can form type I or type II band alignment depending on the core Ga content.[5] Despite progress,[21,22,26] the effect of the microstructure and shell quality on the optoelectronic properties of nanowires has not been studied in depth.

Here, we report a detailed microstructural and optical study of InGaAs/InP core/shell nanowire arrays with different emission wavelengths grown by catalyst-free selective-area metal–organic vapor-phase epitaxy (SA-MOVPE). We identified a window of optimal shell thickness and growth conditions to enhance emission intensity and achieve long minority carrier lifetime. Our optimized core/shell nanowires feature strong core-luminescence of up to 1000 times higher than their bare counterpart and a long minority carrier lifetime of up to 13 ns. The effect of crystal structure on the emission intensity was also investigated using transmission electron microscopy (TEM) and cathodoluminescence (CL) spectroscopy, revealing insights on the role of core and shell thickness.

2. Results and Discussion

Based on our previous report,[12] by changing the growth parameters, uniform InGaAs nanowire arrays with photoluminescence (PL) peak emission from 900 to 1600 nm at 80 K can be grown on patterned GaAs (111)B substrates. At a constant In/(In+Ga) precursors ratio, there is an optimum V/III ratio to grow straight nanowires with the highest aspect ratio (length/diameter) for each growth temperature. For example, at a constant In/(In+Ga) precursors ratio of 0.3, V/III ratios of 2.4, 9, 40, and 80 resulted in high aspect ratio nanowires at growth temperatures of 600, 650, 700, and 750 °C, respectively. These growth conditions resulted in PL emission peaks at 1530, 1420, 1210, and 1120 nm at 80 K, from nanowires grown on patterns with a pitch size of 1 µm and a hole size of 80 nm.[12] Here, InGaAs nanowires with a PL emission peak at 1530 nm (at 80 K) were selected as a representative nanowire array to optimize the InP passivation shell growth, as the matching lattice constant of InGaAs with InP shell leads to the emission of 1550 nm at 80 K.[27] First, the nanowire core was passivated with an InP shell at the same temperature as InGaAs nanowire growth to avoid potential compositional change of the nanowire core and interdiffusion of core/shell interfaces at higher temperatures. Scanning electron microscopy (SEM) image of these nanowires (**Figure 1**a) shows that the InP shell can be grown successfully at 600 °C; however, the uniformity of the nanowire array is reduced. We have observed that at the optimized core growth conditions, the reproducibility and homogeneity of the InGaAs nanowire morphology and optical properties is very high. Our SEM analysis did not identify fluctuations in the nanowire morphology of the as prepared InGaAs cores in different batches. The inhomogeneity of the core-shell arrays at this shell growth temperature was confirmed in two different batches of InGaAs/InP core/shell nanowires. In the presence of a substrate, PH_3 should completely decompose at temperatures above 575 °C.[28] Therefore, the nonuniformity of nanowires morphology might be related to the relatively lower diffusivity of pyrolyzed phosphine at 600 °C than at higher temperatures and/or preferential nonuniform interaction of the arsine precursor with the InGaAs surface at this lower temperature.

To investigate this assumption, InP shell was grown at a higher temperature of 650 °C, while the InGaAs core was grown at 600 °C (a schematic of the core/shell growth sequences can be found in Figure S1a of the Supporting Information). Figure 1b shows uniform InGaAs/InP core/shell nanowires across the entire array with a shell grown at a higher temperature of 650 °C. To study the role of shell growth temperature on the optical properties, PL measurements were carried out at room temperature on these nanowire ensembles grown at the same core growth conditions and different shell growth temperatures of 600 (Figure 1a) and 650 °C (Figure 1b). Red and blue curves in Figure 1c represent the PL spectra from nanowires in Figure 1a,b, respectively. A strong emission peak is observed from both nanowire ensembles at room temperature. However, the PL intensity of the nanowires with a shell grown at 650 °C (Figure 1c, blue line) is five times larger than that with a shell grown at 600 °C (Figure 1c, red line).

Time-resolved PL (TRPL) is an effective tool to extract the minority carrier lifetime, directly representing the material quality. Therefore, it can be employed to determine the optimum growth conditions.[29] The minority carrier lifetime of nanowires with a shell growth temperature of 650 °C is 13 ns, which is more than three times higher than that with a shell growth temperature of 600 °C. Given the comparable nanowire diameters (146 ± 3 nm) and shell thicknesses (23 ± 1 nm) for both shell growth temperatures (Figure 1a,b), the longer minority carrier lifetime can be tentatively assigned to the better qulity of shell or/and better InGaAs/InP shell interface for the shell layer grown at a higher temperature of 650 °C.

A shell growth temperature of 650 °C was chosen to investigate the impact of the InP shell on nanowires grown at different core growth temperatures while minimizing interdiffusion of elements at the core/shell interface. Figure 1d–g shows SEM images of InGaAs/InP core/shell nanowire arrays grown at different core growth temperatures. Figure S1 (Supporting

© 2022 The Authors. Advanced Optical Materials published by Wiley-VCH GmbH

21951071, 2022, 18, Downloaded from https://onlinelibrary.wiley.com/doi/10.1002/adom.202200739 by National Health And Medical Research Council, Wiley Online Library on [05/06/2023]. See the Terms and Conditions (https://onlinelibrary.wiley.com/terms-and-conditions) on Wiley Online Library for rules of use; OA articles are governed by the applicable Creative Commons License

ADVANCED OPTICAL MATERIALS
www.advopticalmat.de

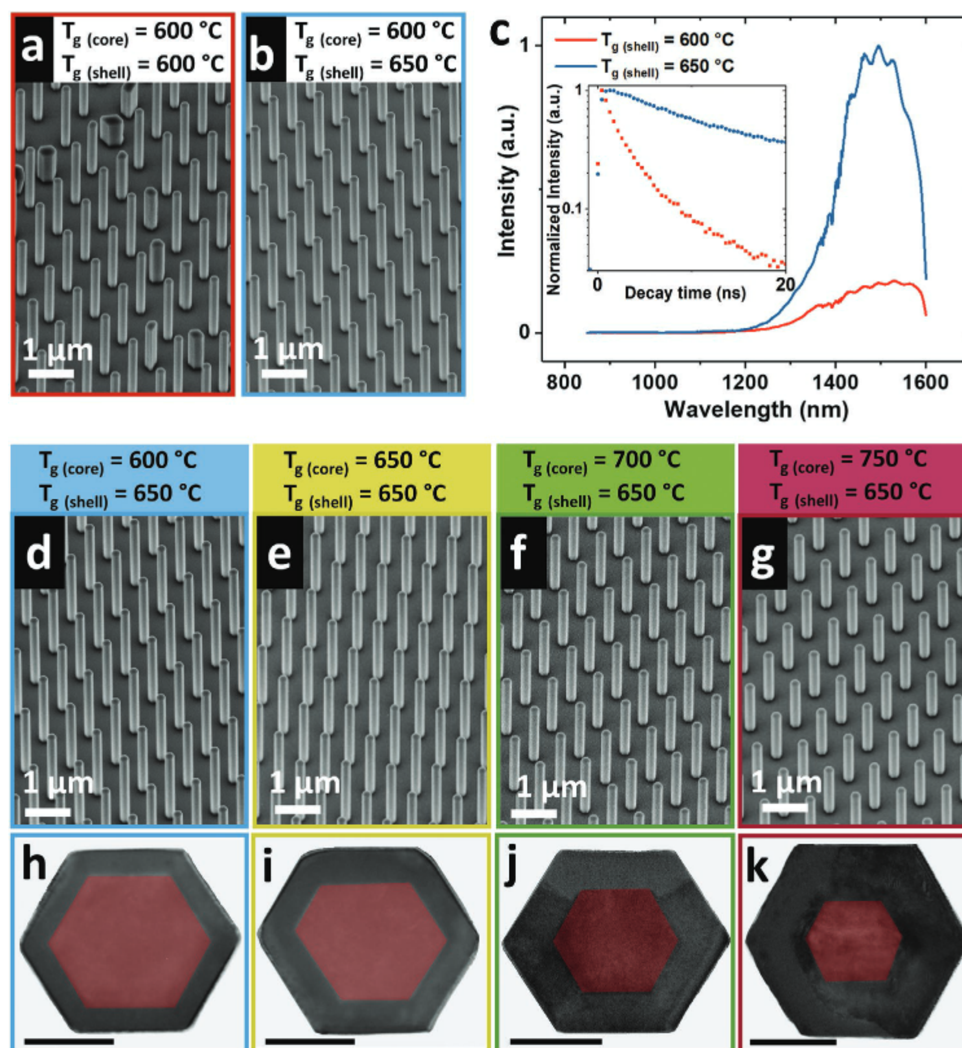

Figure 1. Shell growth optimisation. a–b) SEM images of InGaAs/InP core/shell nanowires with a core grown at 600 °C and V/III ratio of 2.4 and a shell grown at different temperatures of (a) 600 and (b) 650 °C. c) Corresponding PL emission from nanowire arrays with a shell grown at 600 °C (red line) and 650 °C (blue line). The inset compares the PL decay curves of the same nanowires. d–g) SEM images of InGaAs/InP core/shell nanowires grown at different core temperatures and the same shell growth temperature as indicated. h–k) Corresponding cross sectional view of the nanowires. At each core growth temperature, an optimum V/III ratio was selected to grow the nanowires. Scale bars in (h–k) are 50 nm.

Information) shows the schematics of these InGaAs/InP core/shell growth procedures, while Figure S2 (Supporting Information) shows the SEM images of the bare nanowires. The nanowire length/diameter ratios before and after passivation with an InP shell are summarized in Figure S3 (Supporting Information). All the nanowires are highly uniform with a hexagonal cross-section. Cross-sectional scanning transmission electron microscopy (STEM) images (Figure 1h–k) of these nanowires confirmed a uniform shell thickness around the core, although the thickness varies depending on the diameter of the core.

To investigate the compositional uniformity of the core and shell, we conducted EDX–STEM (energy dispersive X-ray STEM) cross-section compositional mapping on the representative nanowires (Figure 1d) that were grown at a core temperature of 600 °C and shell temperature of 650 °C. Cross-sectional STEM image of the nanowires and the corresponding elemental maps reveal a uniform hexagonal core with a uniform shell layer (**Figure 2**a–g). The STEM image along [110] or $[11\bar{2}0]$ zone axis from the middle part of the nanowire (Figure 2h) and the corresponding elemental maps (Figure 2i–n) confirmed the uniform formed shell along the nanowire length.

To investigate the effect of the InP passivation layer on the optical properties of InGaAs nanowires, PL was conducted at 80 K for the bare and passivated nanowires for each growth condition described above. PL was performed across multiple positions on the arrays, resulting in very similar emission spectra. The PL intensity of all the nanowires is increased up to 1000 times after deposition of the passivation layer as can be seen in **Figure 3**. This enhancement indicates a significant passivation of surface states by the InP shell.

Two major effects can be observed in the emission spectra after passivation, namely a narrowing and a shift in the PL emission peak. The enhancement in the PL intensity and linewidth is shown as a function of growth temperature and shell thickness

 © 2022 The Authors. Advanced Optical Materials published by Wiley-VCH GmbH

21951071, 2022, 18, Downloaded from https://onlinelibrary.wiley.com/doi/10.1002/adom.202200739 by National Health And Medical Research Council, Wiley Online Library on [05/06/2023]. See the Terms and Conditions (https://onlinelibrary.wiley.com/terms-and-conditions) on Wiley Online Library for rules of use; OA articles are governed by the applicable Creative Commons License

21951071, 2022, 18, Downloaded from https://onlinelibrary.wiley.com/doi/10.1002/adom.202200739 by National Health And Medical Research Council, Wiley Online Library on [05/06/2023]. See the Terms and Conditions (https://onlinelibrary.wiley.com/terms-and-conditions) on Wiley Online Library for rules of use; OA articles are governed by the applicable Creative Commons License

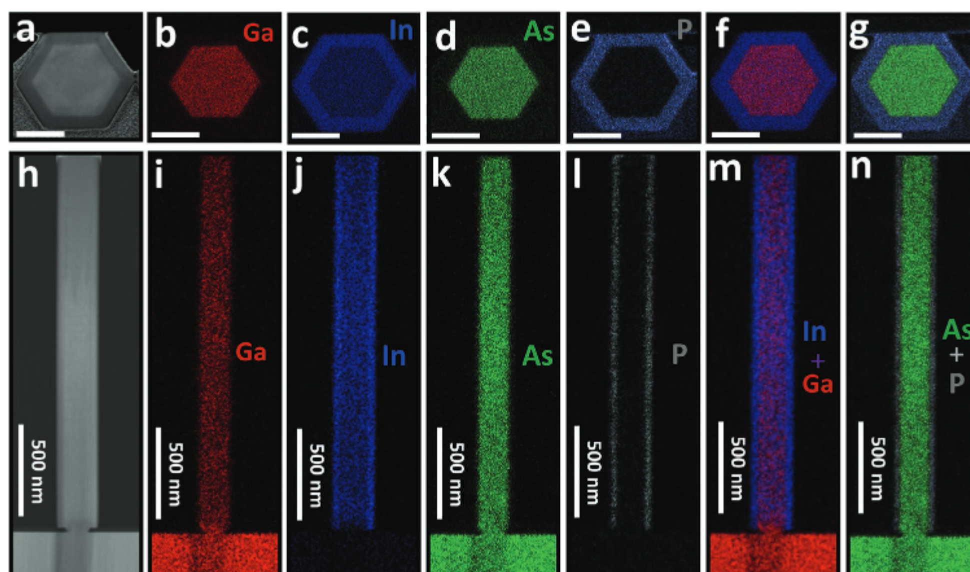

Figure 2. A uniform InP shell on InGaAs nanowire core. a) Cross-sectional STEM image and the corresponding elemental maps of b) Ga, c) In, d) As, e) P, and overlay of f) group III and g) group V elements. The scale bars are 100 nm. h) STEM image of a nanowire along the $[1\bar{1}0]$ or $[11\bar{2}0]$ zone axis and i–n) their corresponding elemental maps as indicated in the images. The InGaAs core was grown at 600 °C and V/III of 2.4, and the shell was grown at 650 °C.

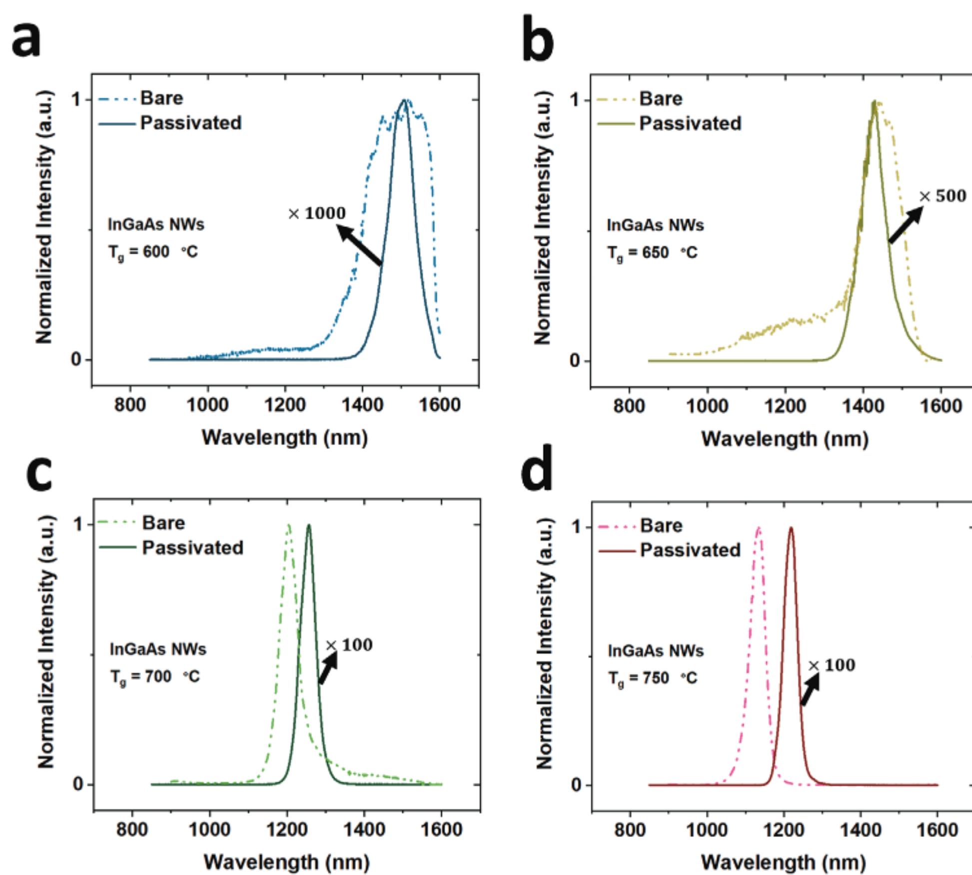

Figure 3. The effect of InP passivation shell on the PL spectrum of InGaAs nanowires with different emission wavelengths for InGaAs nanowires grown at different core growth temperatures of a) $T_g = 600$ °C, b) $T_g = 650$ °C, c) $T_g = 700$ °C, and d) $T_g = 750$ °C with a shell temperature of 650 °C. The arrow labels show the relative intensity increase of the corresponding PL spectra.

© 2022 The Authors. Advanced Optical Materials published by Wiley-VCH GmbH

in Figure S4 (Supporting Information). For the same direct bandgap material, a narrower PL linewidth corresponds to a higher material quality (i.e., lower disorder), which is in line with the higher PL intensity trend observed. Emission peak narrowing after passivation is particularly evident in nanowire cores grown at lower temperatures of 600 and 650 °C. Nanowires grown at 600 °C have an emission peak centered around 1530 nm and show a strong narrowing of the emission peak but no peak shift upon applying the passivation layer (Figure 3a). Based on our previous report, alloy (compositional) fluctuation and local crystal phase variation along the nanowire length can broaden the emission peak. This effect is more pronounced in nanowires grown at lower temperatures that contains a higher In content.[12] Here, the narrower emission peak of the passivated nanowires compared to the bare ones can be assigned to the preferential enhancement of emission from the nanowire core induced by the passivation shell (see Figure 6a–c). In addition, it has been reported that a passivation shell can also reduce surface-related emissions, further narrowing the PL emission peak.[30]

Similarly, passivated nanowire arrays grown at 650 °C (Figure 3b) show a narrower emission peak at 1420 nm and an unvaried emission peak position. It has been reported that $In_{0.53}Ga_{0.47}As$ with an emission wavelength at 1550 nm at 80 K,[27] is latticed matched to InP, resulting in a strain-free InGaAs/InP interface.[31] Here, the invariance of the emission peaks after passivation (Figure 3a,b) indicates a negligible strain at the InGaAs/InP interface at these core growth temperatures (600 and 650 °C).

Figure 3c,d shows a redshift of the emission peak upon passivation for the nanowires with a bare emission peak of 1210 and 1120 nm. These nanowires have a higher content of Ga indicated by their lower emission wavelengths. The observed redshift is attributed to a tensile strain induced by InP passivation layer on InGaAs nanowires.[31] The strain on the $In_xGa_{1-x}As$ core with a high Ga content ($x < 0.5$) could be minimized by replacing InP with InGaP as demonstrated by Kim et al.[20] Their study improved the core/shell interface quality by growing lattice matched InGaP shells on $In_xGa_{1-x}As$ nanowires with different Ga contents.[20] Apart from the Ga content and related lattice mismatch, increasing the shell thickness can also increase the strain in the core, resulting in a larger PL shift.[7] Therefore, the larger redshift of the emission peak in Figure 3d than Figure 3c is partially attributed to the higher thickness of the InP shell (Figure 1k).

To evaluate the uniformity of the nanowire optical properties, CL intensity maps were collected at room temperature along the length of the InGaAs/InP nanowires grown at different growth conditions. **Figure 4**a–d shows the SEM and the corresponding panchromatic CL images of these nanowires. A strong luminescence intensity, peaking in the core of the nanowires, with gradually decreasing intensity toward the sidewalls, is observed for all the nanowires. Despite the strong emission, the intensity

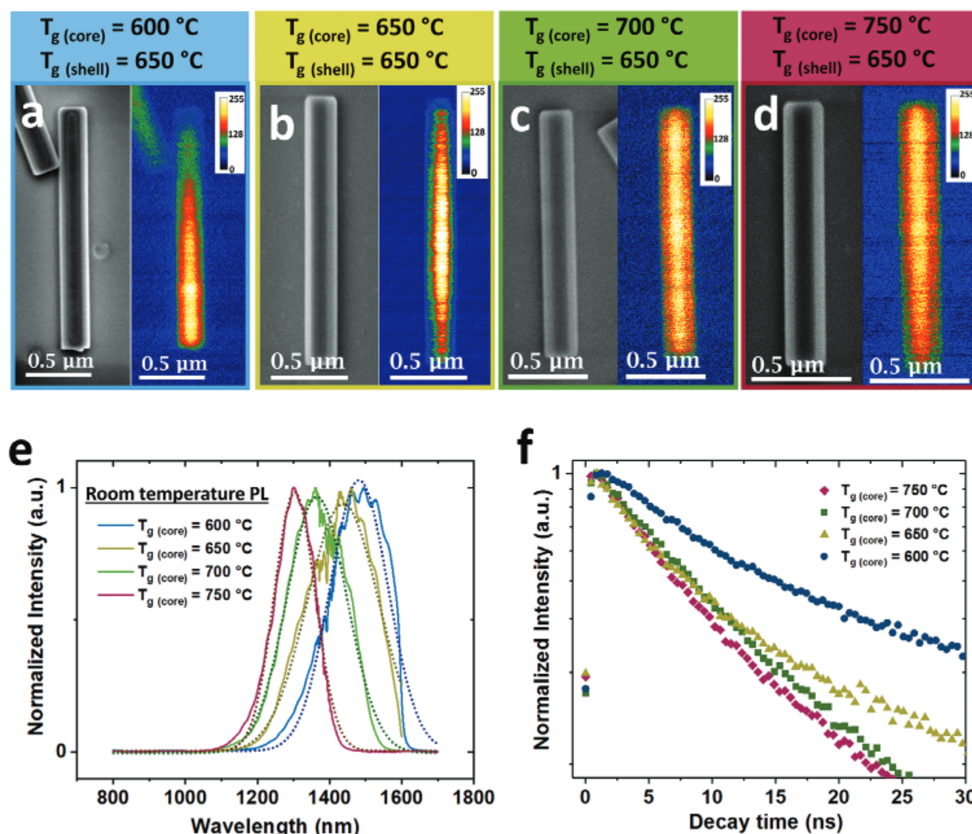

Figure 4. Optical properties of InGaAs/InP nanowires grown under different core temperatures and the same shell growth conditions. SEM and corresponding panchromatic CL images of InGaAs/InP nanowires grown at core growth temperatures of a) 600, b) 650, c) 700, and d) 750 °C and the shell temperature of 650 °C in all cases. Room temperature e) PL emissions and f) time-resolved PL plots of nanowires grown under different growth temperatures (as indicated).

© 2022 The Authors. Advanced Optical Materials published by Wiley-VCH GmbH

21951071, 2022, 18, Downloaded from https://onlinelibrary.wiley.com/doi/10.1002/adom.202200739 by National Health And Medical Research Council, Wiley Online Library on [05/06/2023]. See the Terms and Conditions (https://onlinelibrary.wiley.com/terms-and-conditions) on Wiley Online Library for rules of use; OA articles are governed by the applicable Creative Commons License

is not uniform along the length of the nanowire. This nonuniformity is particularly evident for the nanowire grown with a core growth temperature of 600 °C (Figure 4a), which might be related to the local variation of crystal structure along the nanowire length (*vide infra*). Notably, without passivation, no emission was observed from these nanowires at room temperature.

Figure 4e,f shows the room temperature PL emission and the corresponding PL lifetime from nanowire arrays grown at different core growth temperatures. Figure 4e shows by choosing a suitable nanowire core growth temperature, the emission peak energy of these nanowires can be tuned within the telecommunication wavelengths. All the passivated nanowires (Figure 4f) have long minority carrier lifetime of >9 ns independent of the core growth temperature, with lower core growth temperature resulting in longer minority carrier lifetime. This could be related to the different core diameter, shell thickness, or nanowire crystal structure, as discussed later.

Nanowires grown at a core temperature of 600 °C were selected as representative nanowires to investigate the effect of shell thickness on the minority carrier lifetime. To gain further insights on the mechanisms behind the narrowing of the PL emission peak and shifts in the peak position in Figure 3, time-resolved PL (TRPL) was performed on these samples. Irrespective of the shell thickness, TRPL time decay from all nanowires reveals a single exponential decay (**Figure 5**a). Increasing the shell thickness from 8 to 24 nm increases the minority carrier lifetime, while a further increase to 29 nm decreases the minority carrier lifetime. TRPL was conducted on five spots across the nanowire array for each shell thickness. Figure 5b summarizes the effect of shell thickness on the minority carrier lifetime. The error bars show a small standard deviation of the carrier lifetime across five spots in each nanowire array. An optimum shell thickness of 24 nm results in the highest carrier lifetime of 13 ns. The observed reduction in carrier lifetime with increasing shell thickness might be related to the interdiffusion at the core/shell interface, which has been reported for extended growth time of the shell.[32]

In addition to shell thickness, variation of nanowire core diameter can also affect the carrier lifetime. Figure 5c shows the carrier lifetimes of nanowires with different core diameters and a comparable shell thickness of 24 ± 3 nm. The carrier lifetime increases from 7 to 13 ns with increasing nanowire core diameter from 88 to 164 nm.

The carrier lifetime (τ_{mc}) in a nanowire can be expressed as $\frac{1}{\tau_{mc}} = \frac{1}{\tau_{bulk}} + \frac{4SRV}{d}$, where τ_{bulk} represents the nonradiative recombination decay in bulk InGaAs for a specific composition, SRV is the surface recombination velocity at the InGaAs/InP core/shell interface, and d is the diameter of the InGaAs core. Considering the constant composition of these nanowires (constant τ_{bulk}), we estimated an SRV of ≈280 cm s^{-1} at the InGaAs/InP

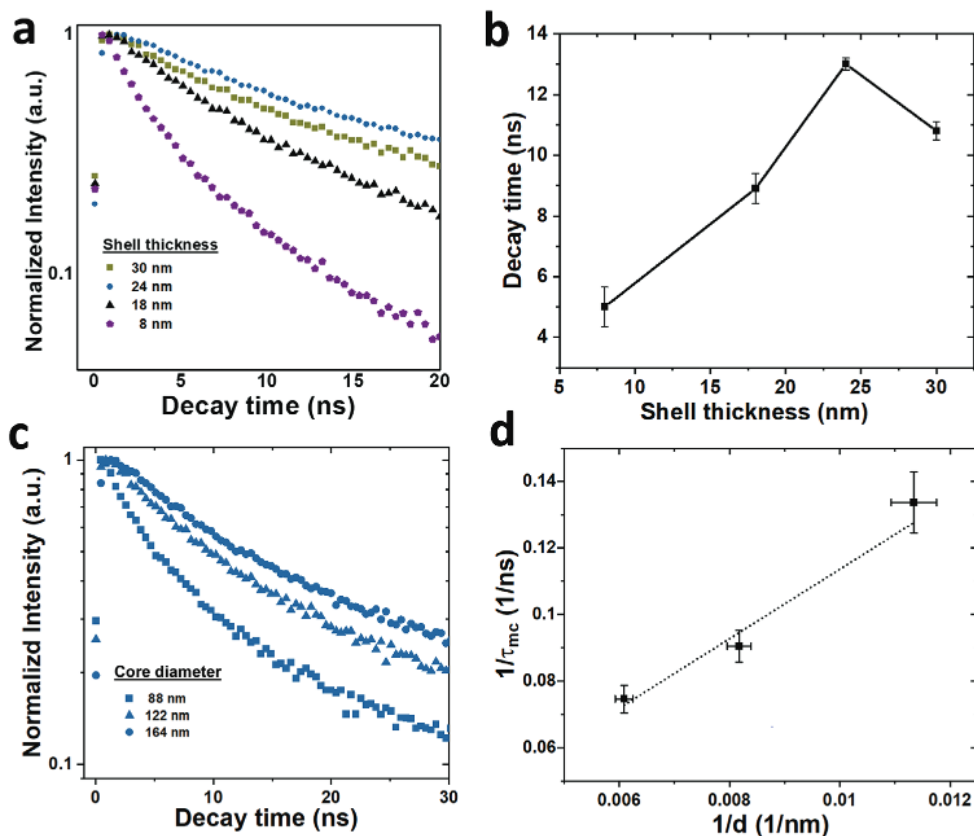

Figure 5. a) Time-resolved PL from nanowires with a shell grown at 650 °C and different thicknesses as indicated. b) Measured τ_{PL} versus shell thickness. c) TRPL from nanowires with comparable shell thickness and different core diameters as labelled. d) Inverse minority carrier lifetime of InGaAs/InP nanowires as a function of inverse nanowire diameter.

© 2022 The Authors. Advanced Optical Materials published by Wiley-VCH GmbH

21951071, 2022, 18, Downloaded from https://onlinelibrary.wiley.com/doi/10.1002/adom.202200739 by National Health And Medical Research Council, Wiley Online Library on [05/06/2023]. See the Terms and Conditions (https://onlinelibrary.wiley.com/terms-and-conditions) on Wiley Online Library for rules of use; OA articles are governed by the applicable Creative Commons License

21951071, 2022, 18, Downloaded from https://onlinelibrary.wiley.com/doi/10.1002/adom.202200739 by National Health And Medical Research Council, Wiley Online Library on [05/06/2023]. See the Terms and Conditions (https://onlinelibrary.wiley.com/terms-and-conditions) on Wiley Online Library for rules of use; OA articles are governed by the applicable Creative Commons License

interface from the linear fit of the inverse PL lifetimes versus the inverse cylindrical diameter of the InGaAs nanowires. To our knowledge, the SRV value is about 50 times lower than the lowest SRV reported for sulphur-treated $In_{0.53}Ga_{0.47}As$ nanostructures.[14] Higuera-Rodriguez et al. report the fabrication of InGaAs rods with diameter between 275 nm and 2.86 µm with a thickness of 350 nm, sandwiched between InP layers and passivated with an SiO_x layer. These InP/InGaAs/InP nanopillars also achieved a low recombination velocity of 260 cm s^{-1}.[26]

The different carrier lifetimes in nanowires with different emission wavelengths (Figure 4f) and the variation in CL intensity along the nanowire length (Figure 4a–d) might be related to the nanowire crystal structure. The crystal structure and the composition of nanowires can also affect optical properties and the SRV. To investigate the cause of nonuniform CL emission intensity along the nanowire length, correlated CL and TEM analysis was carried out on four nanowires, showing consistent results. Figure S5 (Supporting Information) shows that the nanowire shell follows the same stacking sequence as the core. Similar results were observed for all the nanowires independent of the peak emission wavelength. **Figure 6**a,b shows the corresponding panchromatic CL image, CL spectra along the nanowire length and high resolution transmission electron microscopy (HRTEM) of an InGaAs/InP nanowire grown with a core growth temperature of 600 °C on a pattern with a pitch size of 1 µm.

From the base toward the nanowire top, there is a reduction in CL intensity, and the emission spectrum is slightly redshifted (Figure 6b). The redshift of the emission peak could be due to the composition and crystal variation along the nanowire length, which may also induce nonuniform strain on the core. High-resolution TEM from the nanowire top (Figure 6c) shows predominant wurtzite (WZ) structure, while a mixed phase of WZ and zinc blende (ZB) is observed at the nanowire base. A correlation of Figure 6a,c shows a lower emission intensity and slightly longer emission wavelengths in the WZ sections of the nanowires, an indication that the crystal structure plays an important role in the optical properties of InGaAs/InP nanowire.

Ideally, a similar nanowire elemental composition would be required to compare the optical properties of WZ and ZB structures. However, attaining these two structures at a specific In content is very challenging and in SAE grown $In_xGa_{1-x}As$ nanowires, increasing the In content changes the crystal structure

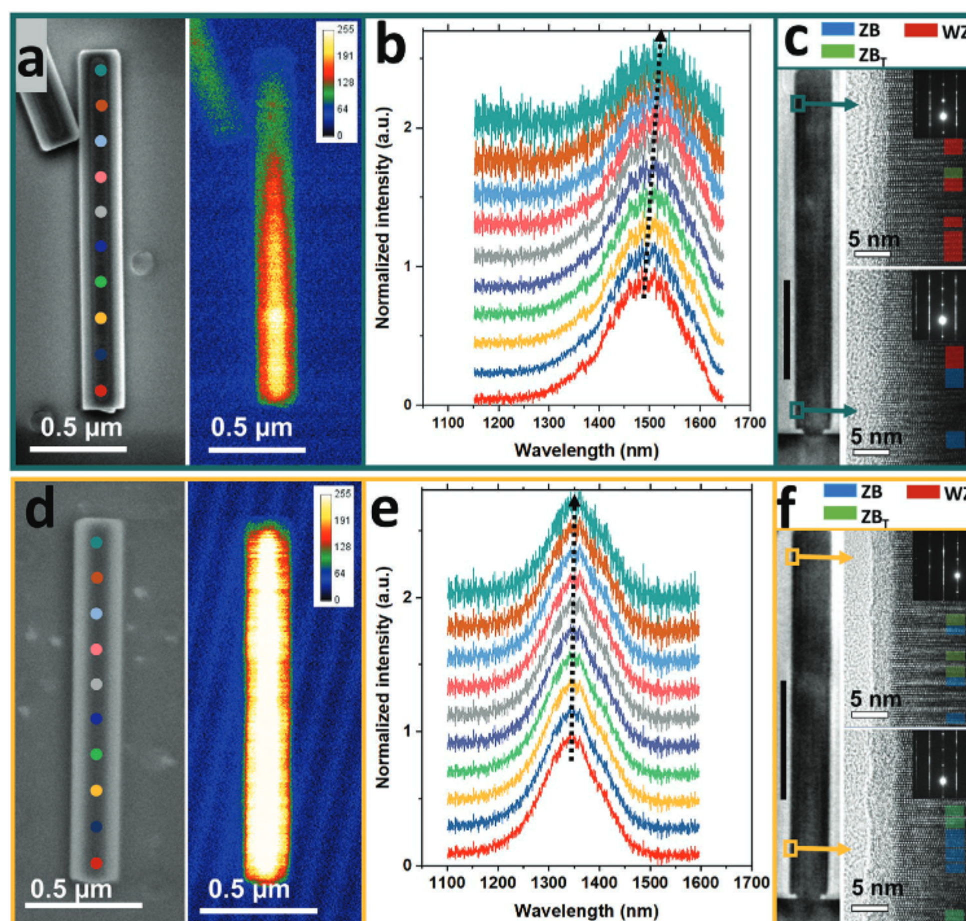

Figure 6. The effect of crystal structure on InGaAs nanowire optical properties. Panels (a) and (d) are the SEM and panchromatic CL images of InGaAs/InP nanowires grown at core growth conditions of 600 °C and V/III ratio of 2.4 and different pitch sizes of a) 0.6 and d) 1 µm. c,e) The CL spectra from the coloured dots along the nanowire in (a) and (d), respectively. Panels (c) and (f) are representative TEM and HRTEM images from the top and base of the nanowires grown at the pitch size of 0.6 and 1 µm, respectively.

 © 2022 The Authors. Advanced Optical Materials published by Wiley-VCH GmbH

from ZB to WZ. Also, changing the core growth temperature for attaining a higher Ga content might affect the number of point defects and consequently impact the CL emission intensity of the nanowires, making it challenging to dissociate the effect of composition from the crystal structure.

In order to minimize the effect of growth temperature on CL emission, the nanowire composition, and hence the emission peak position, was tuned by changing the pattern pitch size for a fixed growth temperature. In order to have a fair comparison between the optical properties of nanowires grown with different pattern pitch sizes, the shell thickness of nanowires grown with a pitch size of 0.6 µm (shell thickness = 22 nm) was tuned to be similar to that of nanowires grown with a pitch size of 1 µm (shell thickness = 24 nm, i.e., samples shown in Figure 6a–c). Figure 6d–f shows respectively the SEM and panchromatic CL images, spectrum along the nanowire length and the HRTEM images of nanowires grown with a pattern pitch size of 0.6 µm. The HRTEM images from the top and base of the nanowire show a predominant ZB structure with a high density of twin defects. The strong CL emission in Figure 6d can be assigned to the dominant ZB structure of the nanowire. In addition, the minority carrier lifetime of the nanowire, having a dominant ZB structure and an optimizing passivated shell thickness of 22 nm, is >13 ns (Figure S6, Supporting Information).

To summarize, we investigated the impact of composition and crystal structure on the emission intensity and carrier lifetime of InGaAs/InP nanowires with emission in telecommunication wavelengths. Our finding shows that the local crystal structure has a predominant role in the resulting optical properties. Nanowires with a predominant ZB crystal structure results in better passivation with a longer minority carrier lifetime and stronger emission intensity.

3. Conclusions

Here, we report the effective passivation of InGaAs nanowire with an InP shell to minimize their surface recombination velocity. We use SA-MOVPE to grow InGaAs nanowire arrays with a fine control of the morphology, composition, and crystal structure. An InP shell was deposited in situ on the nanowires. The optimization of the InGaAs/InP nanowire growth conditions helped to discern the role of nanowire core diameter, shell thickness, nanowire composition, and crystal structure on the optical properties of the nanowires. Optimization of the InP shell results in up to three orders of magnitude increase in the photoluminescence intensity. These optimized InGaAs/InP core/shell nanowires exhibit excellent optical properties with strong PL emissions and a long minority carrier lifetime of up to ≈13 ns at room temperature. A record-low surface recombination velocity of ≈280 cm s^{-1} was measured for InGaAs/InP nanowires with an emission wavelength of 1530 nm. We also observe that the crystal structure impacts the luminescence intensity with CL and HRTEM mapping, showing lower local emission intensities for WZ predominant sections compared to ZB ones. These findings provide directions for engineering high quality nanowires for optoelectronic devices operating in the telecommunication wavelength range.

4. Experimental Section

Prior to GaAs nanowire growth, GaAs (111) B substrates were prepared by first depositing 30 nm-thick SiO_2. Smaller 800 × 800 µm^2 of SiO_2 coated areas were patterned on the substrate using optical lithography and hydrofluoric acid wet-etching. Array pattern with a size of 200 × 200 µm^2 was written in the middle of the square of SiO_2 layer using electron beam lithography followed by reactive ion etching (RIE) of the SiO_2. The lithographic pattern had arrays with different opening diameters of 50, 80, and 120 nm, and pitch sizes of 0.6 and 1 µm. The prepared substrates were loaded into a horizontal flow metal–organic vapor phase epitaxial reactor, and trimethylgallium (TMGa), trimethylindium (TMIn), arsine (AsH_3), and phosphine (PH_3) were used as the precursors of indium, gallium, arsenic, and phosphorus, respectively. Nanowires were grown for 35 min at a constant TMIn/(TMIn+TMGa) ratio of 0.3 and the optimum V/III ratio of 2.4, 9, 40, and 80 at each growth temperature of 600, 650, 700, and 750 °C, respectively. InP passivation shell was then deposited on the nanowire core at 650 °C. Note that during both the core and shell growths, TMIn flow rate was kept constant, and PH_3/TMIn ratio was fixed at 706 for the shell growth. The schematics of the growth steps can be found in Figure S1 (Supporting Information). The morphology of InGaAs nanowires was studied using an FEI-Verios 460 field emission scanning electron microscope (SEM). An EDX system, equipped in the FEI-Verios 460 field emission SEM was used for the elemental analysis of nanowires. For CL characterization, nanowires were broken off the substrate with a glass needle and CL spectroscopic studies were carried out on individual nanowires in the FEI Verios 460 SEM system equipped with a Gatan MonoCL4 Elite module. CL intensity map was collected using a current of 100 pA and an electron excitation voltage of 3 kV. For photoluminescence measurements a HORIBA LabRAM system with a 532 nm laser was used. Nanowire arrays were excited through an objective lens (50×) focused on the top of nanowire arrays (3 µm far from the edges of an array) with measurements done at 80 K. As a result, an ensemble of nanowires was excited parallel to their main axis, and the corresponding luminescence was collected through the same objective lens via a monochromator into an InGaAs detector with a detection range of 800–1600 nm. TRPL experiments were performed using a Horiba system equipped with an InGaAs photomultiplier tube detector with a detection range from 950 to 1600 nm. The excitation source was a picosecond DeltaDiode pulsed laser with a wavelength of 785 nm and a pulse width of 60 ps. The laser was focused onto the samples via a 50× near IR objective. The emission wavelength was selected using a monochromator installed in the detection path. The decay curves were then fitted with a mono-exponential function to extract the lifetime.

The nanowires were physically broken off the substrate with a glass needle and transferred to a TEM grid for EDX and TEM analysis. Both TEM and STEM were carried out using a JEOL 2100F field emission gun transmission electron microscope equipped with STEM capabilities and a SSD detector for STEM-EDX elemental mapping.

Supporting Information

Supporting Information is available from the Wiley Online Library or from the author.

Acknowledgements

The authors thank the Australian Research Council for the financial support and Australian National Fabrication Facility, ACT node, Microscopy Australia, ACT node and Infrastructure Fund from the Australian Centre for Advanced Photovoltaics (ACAP) for access to the facilities used in this work.

Open access publishing facilitated by Australian National University, as part of the Wiley - Australian National University agreement via the Council of Australian University Librarians.

© 2022 The Authors. Advanced Optical Materials published by Wiley-VCH GmbH

21951071, 2022, 18, Downloaded from https://onlinelibrary.wiley.com/doi/10.1002/adom.202200739 by National Health And Medical Research Council, Wiley Online Library on [05/06/2023]. See the Terms and Conditions (https://onlinelibrary.wiley.com/terms-and-conditions) on Wiley Online Library for rules of use; OA articles are governed by the applicable Creative Commons License

Conflict of Interest

The authors declare no conflict of interest.

Data Availability Statement

The data that support the findings of this study are available from the corresponding author upon reasonable request.

Keywords

core/shell nanowires, InGaAs nanowires, selective-area metal–organic vapor-phase epitaxy, surface passivation, ternary semiconductors

Received: March 30, 2022
Revised: April 27, 2022
Published online: June 28, 2022

[1] H.-K. Kang, J. Y. Kim, M.-S. Noh, C.-Y. Kang, Y. D. Kim, M.-H. Cho, J. D. Song, *Nano Energy* **2018**, *53*, 57.
[2] H. Tan, C. Fan, L. Ma, X. Zhang, P. Fan, Y. Yang, W. Hu, H. Zhou, X. Zhuang, X. Zhu, A. Pan, *Nano-Micro Lett.* **2016**, *8*, 29.
[3] K. Chiba, A. Yoshida, K. Tomioka, J. Motohisa, *ACS Photonics* **2019**, *6*, 260.
[4] H. Kim, W. J. Lee, A. C. Farrell, J. S. D. Morales, P. Senanayake, S. V. Prikhodko, T. J. Ochalski, D. L. Huffaker, *Nano Lett.* **2017**, *17*, 3465.
[5] I. Vurgaftman, J. R. Meyer, L. R. Ram-Mohan, *J. Appl. Phys.* **2001**, *89*, 5815.
[6] H. A. Fonseka, A. S. Ameruddin, P. Caroff, D. Tedeschi, M. De Luca, F. Mura, Y. Guo, M. Lysevych, F. Wang, H. H. Tan, A. Polimeni, C. Jagadish, *Nanoscale* **2017**, *9*, 13554.
[7] L. Balaghi, G. Bussone, R. Grifone, R. Hübner, J. Grenzer, M. Ghorbani-Asl, A. V. Krasheninnikov, H. Schneider, M. Helm, E. Dimakis, *Nat. Commun.* **2019**, *10*, 2793.
[8] J. Tatebayashi, Y. Ota, S. Ishida, M. Nishioka, S. Iwamoto, Y. Arakawa, *J. Cryst. Growth* **2013**, *370*, 299.
[9] F. Zhang, X. Zhang, Z. Li, R. Yi, Z. Li, N. Wang, X. Xu, Z. Azimi, L. Li, M. Lysevych, X. Gan, Y. Lu, H. H. Tan, C. Jagadish, L. Fu, *Adv. Funct. Mater.* **2021**, 2103057.
[10] T. Stettner, A. Thurn, M. Döblinger, M. O. Hill, J. Bissinger, P. Schmiedeke, S. Matich, T. Kostenbader, D. Ruhstorfer, H. Riedl, M. Kaniber, L. J. Lauhon, J. J. Finley, G. Koblmüller, *Nano Lett.* **2018**, *18*, 6292.
[11] K. Hiruma, K. Tomioka, P. Mohan, L. Yang, J. Noborisaka, B. Hua, A. Hayashida, S. Fujisawa, S. Hara, J. Motohisa, T. Fukui, *J. Nanotechnol.* **2012**, *2012*, 169284.
[12] Z. Azimi, A. Gopakumar, A. S. Ameruddin, L. Li, T. Truong, H. T. Nguyen, H. H. Tan, C. Jagadish, J. Wong-Leung, *Nano Res.* **2021**, *15*, 3695.
[13] J. Treu, M. Speckbacher, K. Saller, S. Morkötter, M. Döblinger, X. Xu, H. Riedl, G. Abstreiter, J. J. Finley, G. Koblmüller, *Appl. Phys. Lett.* **2016**, *108*, 053110.
[14] M. Boroditsky, I. Gontijo, M. Jackson, R. Vrijen, E. Yablonovitch, T. Krauss, C. C. Cheng, A. Scherer, R. Bhat, M. Krames, *J. Appl. Phys.* **2000**, *87*, 3497.
[15] H. J. Joyce, C. J. Docherty, Q. Gao, H. H. Tan, C. Jagadish, J. Lloyd-Hughes, L. M. Herz, M. B. Johnston, *Nanotechnology* **2013**, *24*, 214006.
[16] Z. Azimi, N. Gagrani, J. Qu, O. L. C. Lem, S. Mokkapati, J. M. Cairney, R. Zheng, H. H. Tan, C. Jagadish, J. Wong-Leung, *Nanoscale Horiz.* **2021**, *6*, 559.
[17] K. W. Ng, W. S. Ko, R. Chen, F. Lu, T. T. D. Tran, K. Li, C. J. Chang-Hasnain, *ACS Appl. Mater. Interfaces* **2014**, *6*, 16706.
[18] K. Komolibus, A. C. Scofield, K. Gradkowski, T. J. Ochalski, *Appl. Phys. Lett.* **2016**, *108*, 061104.
[19] A. G. Saraswathy Vilasam, P. K. Prasanna, X. Yuan, Z. Azimi, F. Kremer, C. Jagadish, S. Chakraborty, H. H. Tan, *ACS Appl. Mater. Interfaces* **2022**, *14*, 3395.
[20] H. Kim, W. J. Lee, A. C. Farrell, A. Balgarkashi, D. L. Huffaker, *Nano Lett.* **2017**, *17*, 5244.
[21] H. Kim, W. Lee, T. Chang, D. L. Huffaker, *Phys. Status Solidi – Rapid Res. Lett.* **2019**, *13*, 1800489.
[22] A. S. Ameruddin, H. A. Fonseka, P. Caroff, J. Wong-Leung, R. L. O. H. Veld, J. L. Boland, M. B. Johnston, H. H. Tan, C. Jagadish, *Nanotechnology* **2015**, *26*, 205604.
[23] J. Treu, T. Stettner, M. Watzinger, S. Morkötter, M. Döblinger, S. Matich, K. Saller, M. Bichler, G. Abstreiter, J. J. Finley, J. Stangl, G. Koblmüller, *Nano Lett.* **2015**, *15*, 3533.
[24] J. Treu, M. Bormann, H. Schmeiduch, M. Döblinger, S. Morkötter, S. Matich, P. Wiecha, K. Saller, B. Mayer, M. Bichler, M. C. Amann, J. J. Finley, G. Abstreiter, G. Koblmüller, *Nano Lett.* **2013**, *13*, 6070.
[25] Q. Gao, D. Saxena, F. Wang, L. Fu, S. Mokkapati, Y. Guo, L. Li, J. Wong-Leung, P. Caroff, H. H. Tan, C. Jagadish, *Nano Lett.* **2014**, *14*, 5206.
[26] A. Higuera-Rodriguez, B. Romeira, S. Birindelli, L. E. Black, E. Smalbrugge, P. J. van Veldhoven, W. M. M. Kessels, M. K. Smit, A. Fiore, *Nano Lett.* **2017**, *17*, 2627.
[27] L. M. Casson, F. Ndi, E. Teboul, *MRS Proc.* **2009**, *1195*, 1195.
[28] R. Lückerath, P. Tommack, A. Hertling, H. J. Koss, P. Balk, K. F. Jensen, W. Richter, *J. Cryst. Growth* **1988**, *93*, 151.
[29] R. K. Ahrenkiel, *Solid State Electron* **1992**, *35*, 239.
[30] M. H. Sun, H. J. Joyce, Q. Gao, H. H. Tan, C. Jagadish, C. Z. Ning, *Nano Lett.* **2012**, *12*, 3378.
[31] S. J. Sweeney, T. D. Eales, A. R. Adams, *J. Appl. Phys.* **2019**, *125*, 082538.
[32] N. Jiang, Q. Gao, P. Parkinson, J. Wong-Leung, S. Mokkapati, S. Breuer, H. H. Tan, C. L. Zheng, J. Etheridge, C. Jagadish, *Nano Lett.* **2013**, *13*, 5135.

© 2022 The Authors. Advanced Optical Materials published by Wiley-VCH GmbH

21951071, 2022, 18, Downloaded from https://onlinelibrary.wiley.com/doi/10.1002/adom.202200739 by National Health And Medical Research Council, Wiley Online Library on [05/06/2023]. See the Terms and Conditions (https://onlinelibrary.wiley.com/terms-and-conditions) on Wiley Online Library for rules of use; OA articles are governed by the applicable Creative Commons License